Available online at www.sciencedirect.com

SciVerse ScienceDirect

Acta Materialia 61 (2013) 5263–5277

Acta MATERIALIA

www.elsevier.com/locate/actamat

# Evolution of texture and microstructure during hot torsion of a magnesium alloy

Somjeet Biswas [a,b], Benoît Beausir [b,c], Laszlo S. Toth [b,c,*], Satyam Suwas [a]

[a] Department of Materials Engineering, Indian Institute of Science, Bangalore 560 012, India
[b] Laboratory of Excellence on Design of Alloy Metals for Low Mass Structures, Université de Lorraine, Metz, France
[c] Laboratoire d'Étude des Microstructures et de Mécanique des Matériaux, UMR 7239, CNRS/Université de Lorraine, F-57045 Metz, France

Received 13 April 2013; received in revised form 15 May 2013; accepted 16 May 2013
Available online 19 June 2013

**Abstract**

A systematic study of the evolution of the microstructure and crystallographic texture during free end torsion of a single phase magnesium alloy Mg–3Al–0.3Mn (AM30) was carried out. The torsion tests were done at a temperature of 250 °C to different strain levels in order to examine the progressive evolution of the microstructure and texture. A detailed microstructural analysis was performed using the electron back-scattered diffraction technique. The observed microstructural features indicated the occurrence of continuous dynamic recovery and recrystallization, starting with the formation of subgrains and ending with recrystallized grains with high angle boundaries. Texture and microstructure evolution were analysed by decoupling the effects of imposed shear and of dynamic recrystallization. Microstructure was partitioned to separate the deformed grains from the recovered/recrystallized grains. The texture of the deformed part could be reproduced by viscoplastic self-consistent polycrystal simulations. Recovered/recrystallized grains were formed as a result of rotation of these grains so as to reach a low plastic energy state.


*Keywords:* Torsion; Magnesium; Texture; Dynamic recrystallization; Continuous dynamic recovery

## 1. Introduction

Wrought magnesium alloys are considered as potential materials to be used in eco-conscious automobile, aerospace and other lightweight structures due to their low density, superior specific stiffness and strength over other metals and alloys [1,2]. The practical use of these alloys requires shape forming, where the material is subjected to very large plastic deformation, preferably at high temperatures. Large plastic deformation, in addition to obtaining a desired shape, can be used to tailor an optimal microstructure and crystallographic texture. This could lead to improvements in the properties of these alloys and, hence, their performance. It is, therefore, necessary to examine the deformation behaviour of Mg alloys up to very large strains.

Tensile tests are unable to provide large deformations, since uniform deformation is limited due to strain localization leading to necking. However, it is possible to achieve large deformations without rupture or strain localization by free end torsion testing. The behaviour of materials under torsion is quite well known for cubic materials [3–8] as well as for some hexagonal closed packed (hcp) metals like zirconium [9] and titanium [10,11]. A few studies carried out by some of the present authors were directed at the examination of the evolution of texture in magnesium alloys during torsion [12,13]. While deformation texture evolution was examined in a comprehensive manner and was modelled using the viscoplastic self-consistent (VPSC) polycrystal model in these papers, the role of accompanying thermal processes, like recovery or recrystallization, were not addressed.

* Corresponding author at: Laboratoire d'Étude des Microstructures et de Mécanique des Matériaux, UMR 7239, CNRS/Université de Lorraine, F-57045 Metz, France. Tel.: +33 604528208; fax: +33 387315366..
*E-mail address:* laszlo.toth@univ-lorraine.fr (L.S. Toth).

1359-6454/$36.00 
http://dx.doi.org/10.1016/j.actamat.2013.05.018

It is well known that processing of magnesium at elevated temperature (>200 °C) is predominantly accompanied by recovery and dynamic recrystallization (DRX) [14,15]. The exact mechanism, however, is not yet uniquely agreed [15–19]. A recent work by the present authors [20] revealed that the DRX mechanism in magnesium is rather orientation dependent. It was proposed by Biswas et al. [20] that differences in the stacking fault energies between the basal and non-basal crystallographic planes play an important role in the continuous dynamic recovery and recrystallization processes at temperatures ranging from room temperature up to 250 °C.

It is well known that the recrystallization texture of hcp metals can be interpreted by rotations of ~30° around the $c$ axis or by about ~90° around $\{10\bar{1}0\}$ [21–26]. However, Gottstein et al. [22,27], Suwas et al. [28–30] and Wagner et al. [31] have shown independently that for magnesium alloys, $Ti_3Al$ and titanium the recrystallization texture is identical to the deformation texture. Retention of the deformation texture is said to be due to either extensive recovery and polygonization or reorientation of the nuclei. Gottstein et al. [27] have revealed that during annealing of magnesium alloys there is a growth preference for nuclei rotated by ~30° around the $c$ axis from $\langle 11\bar{2}0\rangle$ to $\langle 10\bar{1}0\rangle$. This 30° rotation can be seen in the orientation distribution functions (ODFs). The question is it due to discontinuous dynamic recrystallization (DDRX) or continuous dynamic recrystallization (CDRX)?

The present work aims at examining the evolution of the microstructure and texture during hot deformation of Mg alloy AM30 at a fixed temperature and strain rate as a function of strain. Samples were deformed to different strain levels by torsion and analysed by scanning electron microscopy (SEM) based electron back-scattered diffraction (EBSD). The torque was measured as a function of twist angle, from which the strain hardening curve was constructed. A twisting rate of 0.001 rad $s^{-1}$ and temperature of 250 °C were chosen because under these conditions large plastic strain and DRX are favoured. VPSC simulations were performed to understand the measured mechanical behaviour and evolution of the texture. The effect of dynamic recovery/recrystallization was interpreted by analysing the plastic energy in the orientation space.

## 2. Experiments

Free end torsion tests were carried out on extruded solid bars of Mg alloy AM30 with the composition 3.2 wt.% Al, 0.3 wt.% Mn, balance Mg. Samples for torsion testing with a length of 38 mm and diameter of 6 mm were prepared from these extruded rods with the longitudinal axis parallel to the extrusion direction (for more information on the samples see Beausir et al. [13]). The average grain size of the as-received material was ~25 μm (Fig. 1a). The initial texture was axisymmetric with respect to the axial direction of the samples, displayed in an inverse pole figure in Fig. 1b.

Torsion tests were carried out in a specially designed computer controlled apparatus with axial freedom of motion in a vertical set-up. The samples were fixed to grips with the help of three screws at each end. Due to the weight of the axial bearing the samples were subjected to a constant axial loading of about 10 N, however, this load represented an axial stress of only about 0.35 MPa, which was practically negligible with respect to the flow stress of the material. The frictional forces for twisting were also negligibly small with respect to the measured torque. The torque and the axial strain were measured as a function of the twist angle.

The samples were heated slowly up to 250 °C. Twisting started immediately after the temperature was attained and the tests were interrupted after deformation to the desired level. Seven tests were carried out at a temperature of 250 °C and a revolution rate of $10^{-3}$ rad $s^{-1}$ (shear strain rate $7.5 \times 10^{-4}$ $s^{-1}$) to different strain levels, leading to fracture at the maximum strain. After testing the samples were rapidly cooled in water. The microstructures and the textures before and after deformation were measured by EBSD in a field emission gun equipped scanning electron microscope. The EBSD measurements were carried out on longitudinal sections of the samples (parallel to the axis of the cylinder). The surfaces were first mechanically polished, followed by electrolytic polishing [20].

## 3. Results and discussions

### 3.1. General features of deformation and stress–strain curves

The twisted bar maintained its perfect cylindrical geometry without any corrugation of its surface during torsion for all strain levels, showing that the sample remained axisymmetric during the test. The maximum shear strain that could be reached before fracture at 250 °C was $\gamma \approx 1.73$. The variation in sample length due to the Swift effect [32,33] is presented in Fig. 2. A shortening was observed, attaining a maximum of about −6% at a shear strain of approximately $\gamma \approx 1.35$. Beyond this strain level shortening stopped.

Fig. 3 displays the torque–twist angle curve. The circles on the plot correspond to the different torque and twist angles at which the tests were stopped to examine the microstructure and texture. The shear stress–shear strain plots were obtained from the measured torque–twist angle curves using the Fields and Backofen formula [34]:

$$\tau_a = \frac{T}{2\pi a^3}\left[3 + \left.\frac{\partial \ln T}{\partial \ln \theta}\right|_{\dot{\theta}} + \left.\frac{\partial \ln T}{\partial \ln \dot{\theta}}\right|_{\theta}\right] = \frac{T}{2\pi a^3}[3 + n + m] \qquad (1)$$

Here $\tau_a$ is the shear flow stress at the outer radius $a$ of the bar, $T$ is the torque, and $\theta$ is the twist angle. The shear strain was calculated from the angle of rotation and refers to the outer radius of the sample. In the present work the tests were carried out at only one strain rate ($\dot{\theta}$ = 0.001 rad $s^{-1}$), so the strain rate sensitivity parameter

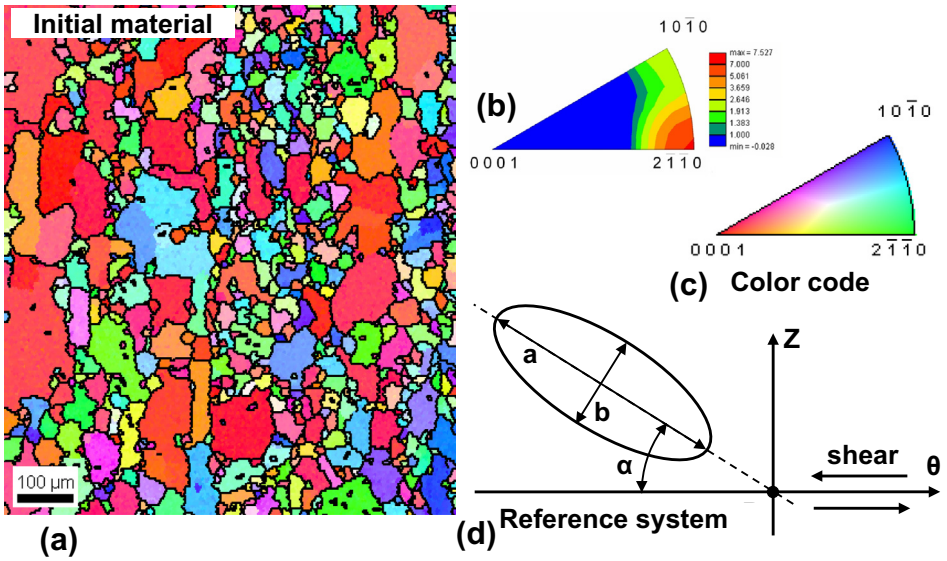


Fig. 1. (a) Inverse pole figure of the initial material, which was in the form of extruded rods (the $z$-axis is the extrusion direction). (b) Inverse pole figure of the extrusion direction ($z$-axis) showing the texture of the starting material. (c) Colour code. (d) Reference system also showing schematically the formation of elliptical grains during shear deformation.

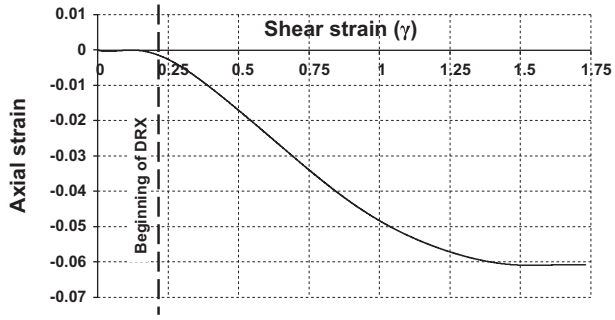


Fig. 2. Shear strain vs. axial strain curve of AM30 during a free end torsion test at 250 °C and strain rate of $7.5 \times 10^{-4}$ s$^{-1}$.

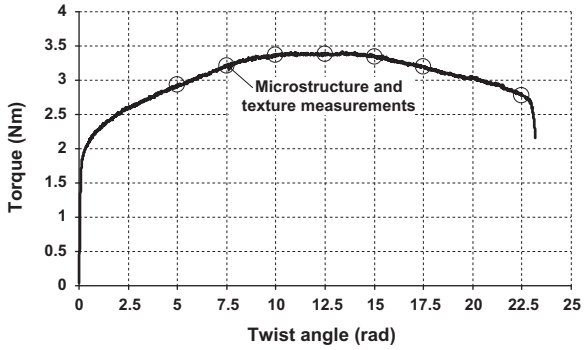


Fig. 3. Measured twist angle vs. torque curve of AM30 during free end torsion at 250 °C at a shear strain rate of $7.5 \times 10^{-4}$ s$^{-1}$. The circles indicate places where the microstructure and the texture were examined.

$m$, which is the third term in Eq. (1), was measured by strain rate jump tests. An average value of $m = 0.2$ was obtained, which is in agreement with the range given in

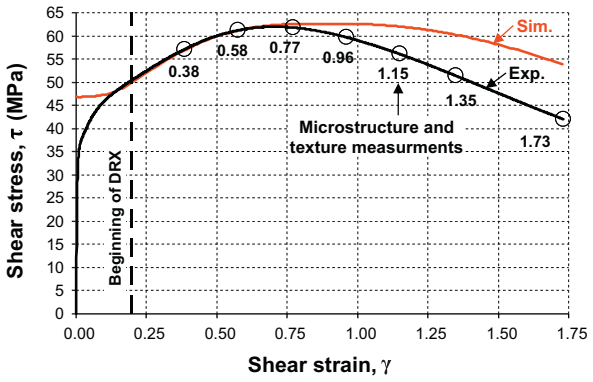


Fig. 4. Shear stress vs. shear strain curve obtained from the measured twist angle vs. torque curve in Fig. 3.

the literature [35,36]. Fig. 4 shows the obtained shear stress–shear strain curve. It can be seen from the figure that the shear stress increases with strain up to a strain level of $\gamma \approx 0.7$. On increasing the strain beyond this the shear stress decreases, leading to fracture at $\gamma \approx 1.73$. It is anticipated that the decrease in shear stress is associated with some dynamic restoration process, presumably DRX (confirmed posteriori). To determine the beginning of DRX, the method of Poliak and Jonas [37] was employed, where the onset of DRX corresponds to an inflexion point in the second derivative of the strain hardening curve. Fig. 5 presents the conventional strain hardening rate $\theta = (\partial\tau/\partial\gamma)_{\varepsilon}$ and its derivative $\theta^* = -(\partial\theta/\partial\tau)_{\varepsilon}$ with respect to the shear stress at a constant strain rate. The minimum of the derivative of the rate of hardening appears at a shear stress of 50 MPa, corresponding to a shear strain of $\gamma \approx 0.2$ (shown also in Fig. 4).

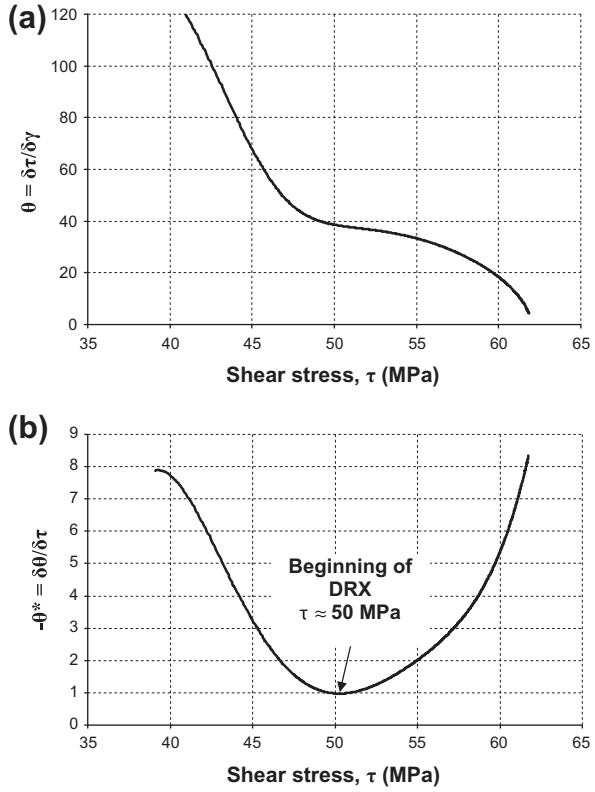


Fig. 5. The (a) first and (b) second derivatives of the torsion stress–strain curve.

### 3.2. Microstructural evolution

The microstructure of the starting material (Fig. 1a) is characterized by a mixture of equiaxed and elongated grains (in the axial $\{z\}$ direction). Fig. 6a displays IPFs of the microstructure at different shear strain levels between 0.38 and 1.73. It can be seen that some of the grains are elongated and oriented at a certain angle to the shear direction ($\theta$). In addition, many small and equiaxed grains having serrated grain boundaries are present, forming a necklace-like structure.

Fig. 7 shows the grain size distribution for the starting as well as the maximum deformed sample as both area and number fraction statistics. Due to the presence of some large grains the distribution was found to be bimodal for both the initial and deformed samples in the area fraction representation. The number fraction distribution is unimodal because the small grains are far more numerous than the few large ones. The average grain sizes corresponding to these two types of distributions were ~80 and ~20 μm from the area fraction calculations and ~23 and ~3.7 μm from the number fraction measurements for the initial and maximum deformed samples, respectively. Thus significant grain size refinement took place during torsion of this Mg alloy.

In order to carry out further analyses the microstructures were partitioned between deformed and (presumably) dynamically recrystallized grains. The bimodal grain size distribution with a minimum at ~10 μm for all the microstructures was used for the partition. Thus grains smaller than 10 μm were considered to be dynamically recrystallized grains and those larger than 10 μm were taken to be deformed ones. The partitioned microstructures are shown in Fig. 6, in which column (a) presents the overall microstructure, column (b) the dynamically recovered/recrystallized grains, and column (c) the deformed grains. In order to ensure that this partitioning was correct, two further criteria were taken into account.

1. The shapes of the partitioned grains were analysed for each condition. The grains smaller than 10 μm were found to be equiaxed (Fig. 6b), while the larger grains were elongated (Fig. 6c). In order to analyse the shape of the larger grains (Fig. 6c) the theoretical change in shape of the grains was calculated as a function of shear strain. The spherical shape of the initial grains became ellipsoidal after torsion, so the orientation and shape of the elliptical grain can be related to the amount of shear according to the relation [38]:

$$a/b = 0.5(2 + \gamma^2 + \gamma\sqrt{\gamma^2 + 4}) \quad (2)$$

$$\tan 2\alpha = 2/\gamma \quad (3)$$

where $a$ and $b$ are the major and minor axes of the ellipse and $\alpha$ is the angle between the shear direction and the major axis of the grain (see schematic shape in Fig. 1d). The theoretical shapes and orientations calculated for each deformation level are superimposed on Fig. 6c, where the ellipse represents the shape (only the morphology, not the size) and their orientation is the measure of strain. The agreement between the theoretical prediction of grain shape and the experimental measurements appear quite satisfactory, supporting the criterion adopted to separate the deformed grains from the dynamically recovered/recrystallized ones.

2. The partitioned small grains showed a rotation of the texture component from $\varphi_2 = 0°$ or 60° to 30° for the large elongated grains (see Section 3.5), which will be discussed in Section 3.6. This also indicates the appropriateness of partitioning the microstructure into dynamically recrystallized and deformed grains.

Using the data displayed in Fig. 6 it is possible to calculate the area fraction of the dynamically recrystallized and deformed grains, the results of which are displayed in Fig. 8. It can be seen that the fraction of dynamically recrystallized grains increases with straining and, consequently, the volume fraction of the deformed grains decreases. Almost half of the grains were dynamically recrystallized before fracture. Furthermore, the microstructural features indicate that smaller equiaxed grains surround the elongated ones, indicating the formation of "necklaces" of dynamically recrystallized grains on the pre-existing grain boundaries. With an increase in strain bands consisting of dynamically recrystallized grains were observed which became thicker. Fig. 9 shows the average number of small equiaxed dynamically recrystallized grains

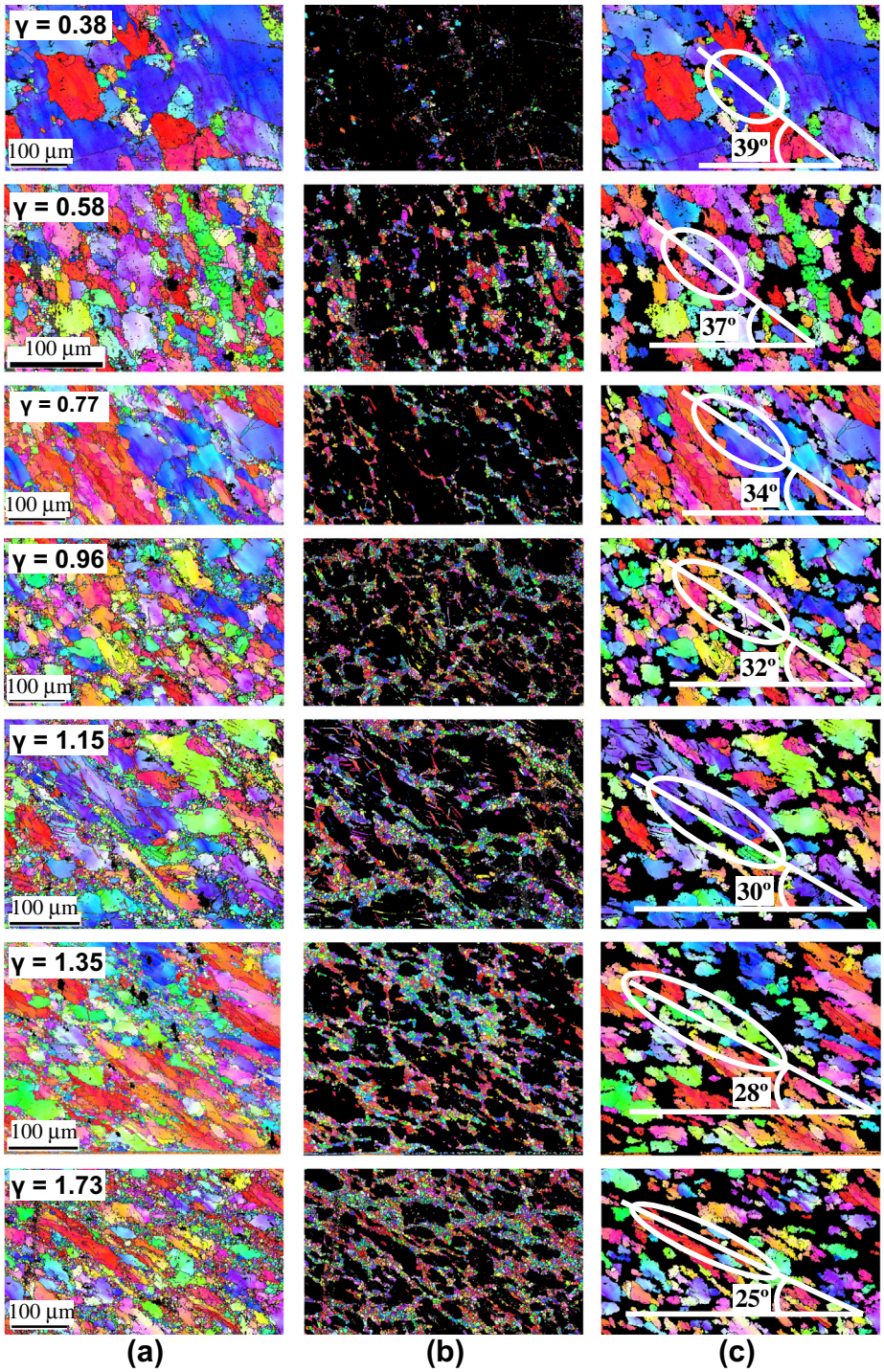


Fig. 6. Inverse pole figures of the torsion tested samples at different strain levels. (a) The entire microstructure, (b) the dynamically recrystallized part and (c) the deformation part. The $z$ axis is vertical, the $\theta$ axis is horizontal, with shear in the negative $\theta$ direction.

that surround deformed grains as a function of strain. As be seen, this number increases from ~14 at $\gamma = 0.38$ to ~35 at $\gamma = 1.73$.

The average grain size evolution is presented in Fig. 10. This figure gives both the average size of the dynamically recrystallized and deformed grains. The grain size of the overall microstructure decreased continuously with strain, leading to an average grain size of ~20 μm after a shear of 1.73 according to the area fraction and of ~3.7 μm according to the number fraction calculations. The average grain size of the dynamically recrystallized grains remained almost constant for all strain levels, at ~5 μm for the area fraction and ~3.2 μm for the number fraction calculations. For the deformed grains the grain sizes were always in the range 35–130 μm by area fraction and 20–30 μm by number fraction.

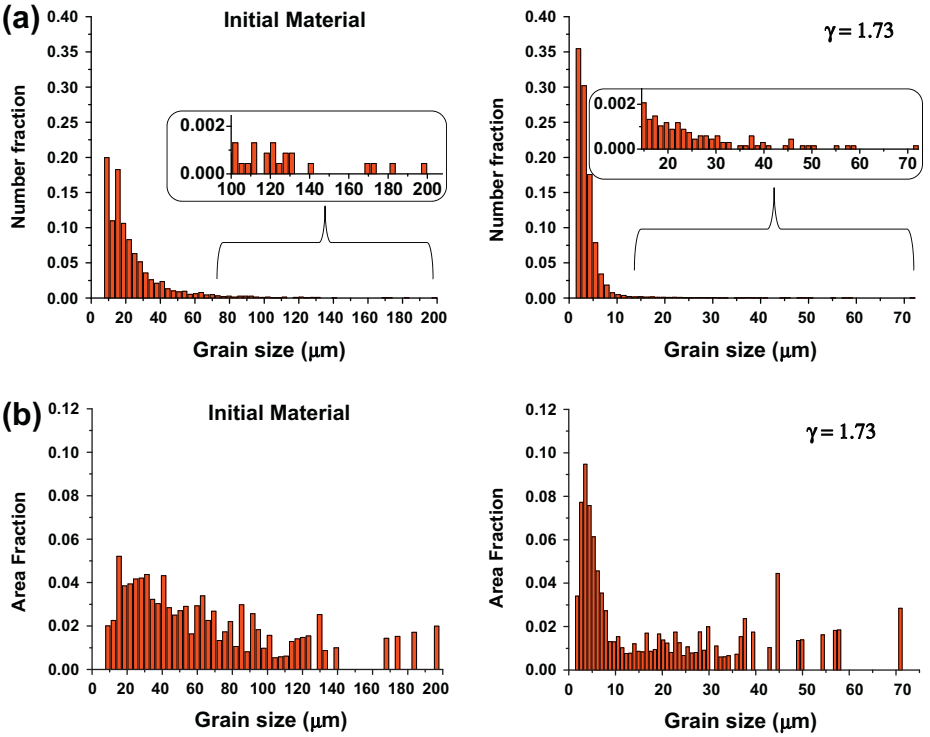


Fig. 7. Grain size distribution for the starting material and at fracture of the torsion samples. (a) Area fraction. (b) Number fraction.

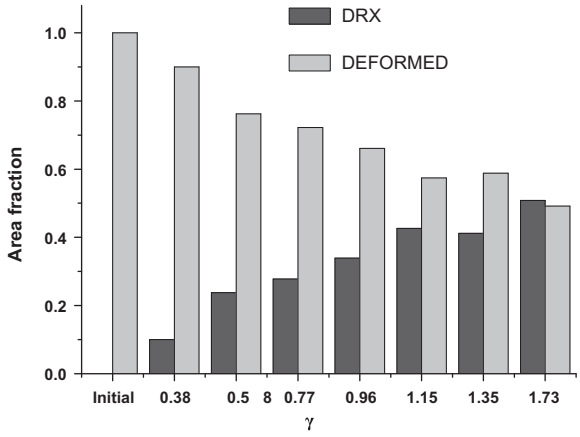


Fig. 8. Area fraction of dynamically recrystallized grains and deformed grains as a function of shear strain.

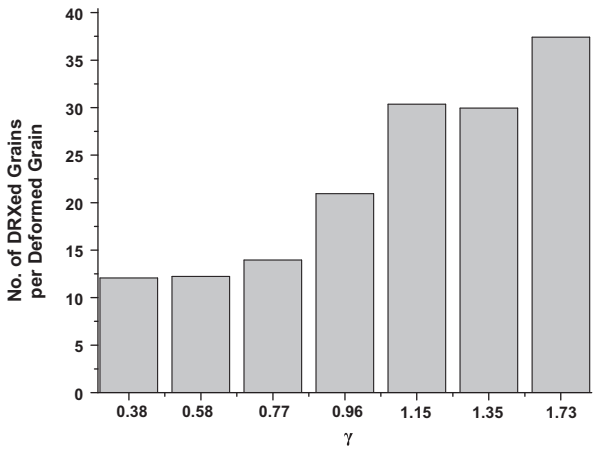


Fig. 9. Average number of dynamically recrystallized grains per deformed grain as a function of shear strain.

The fractions of low angle grain boundaries (LAGB), high angle grain boundaries (HAGB) and twin boundaries are plotted as a function of strain in Fig. 11. The proportion of LAGB is dominant up to a strain of $\gamma = 0.77$. At larger strains the HAGB fraction becomes predominant, the transition occurring at a shear strain between $\gamma = 0.77$ and 0.96. A significant increase in the number of dynamically recrystallized grains (Fig. 9) also occurred in this strain range. From these results it is clear that the morphology changed significantly at a shear strain of about 1.0. Observations of the mechanical behaviour of the samples (Fig. 4) indicated that softening begins at a shear strain of about 0.77.

The fraction of twin boundaries is also reported on Fig. 11a. Three types of twins can form in magnesium: (i) $\{10\bar{1}2\}$ tensile twins (TT) with an 86° $\langle 11\bar{2}0\rangle$ orientation relationship between the twin and the matrix; (ii) $\{10\bar{1}1\}$ compression twins (CT) with the orientation relationship of 56° $\langle 11\bar{2}0\rangle$; (iii) the $\{10\bar{1}1\}$–$\{10\bar{1}2\}$ secondary twins (ST) with a 38° $\langle 11\bar{2}0\rangle$ rotation between the twin variants and the untwined matrix [39]. Very low fractions of CT and ST were observed (~0.1–0.4%). The fraction of TT increased with strain up to ~6% at $\gamma = 1.15$, then decreased until fracture. Fig. 12 shows the grain boundary map at the strain $\gamma = 1.15$, highlighting the twin boundaries. A sudden

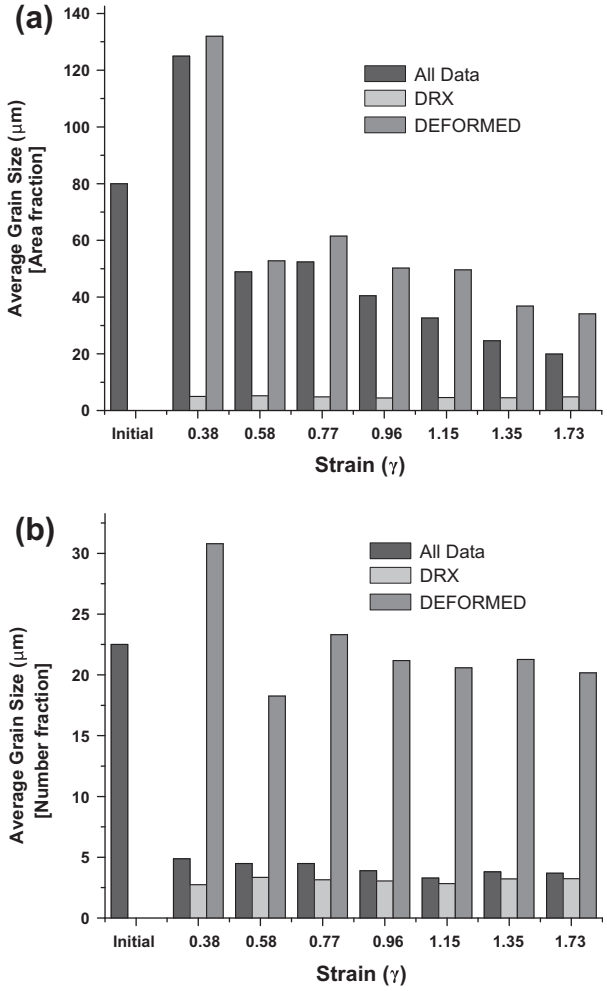


Fig. 10. Average grain size as a function of shear strain corresponding to (a) the area fraction and (b) the number fraction.

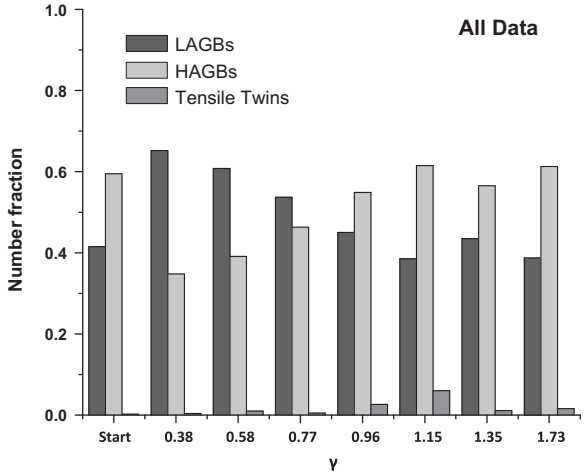


Fig. 11. Grain boundary character distribution as a function of shear strain.

increase in the TT fraction indicates a significant contribution of these twins to the deformation mechanism in this strain regime.

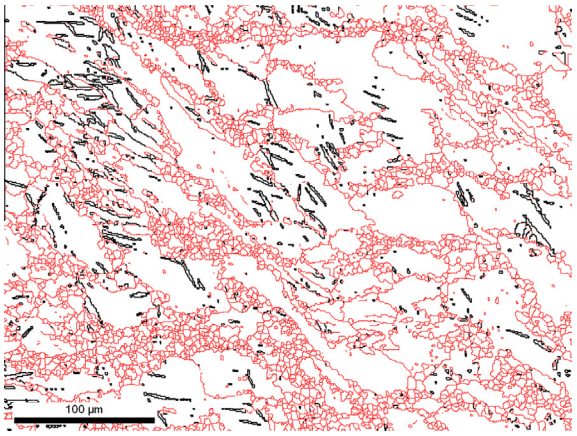


Fig. 12. Grain boundary map of magnesium strained $\gamma = 1.15$ showing tensile and compression twins in black and grain boundaries in red.

### 3.3. Texture analysis

The textures were determined from EBSD measurements. Sufficiently large areas were scanned each time to obtain statistical accuracy. Fig. 13 displays $(10\bar{1}0)$, $(11\bar{2}0)$ and $(0002)$ pole figures derived from the EBSD measurements. In all pole figures the projection plane is the plane with normal $R$ (the radial axis), the shear direction is horizontal ($\theta$ axis) towards the left and the axial direction ($Z$) is vertical (the same reference system as in Fig. 1a). In order to confirm that the microtexture measurements are representative, bulk texture measurements were also carried out on the $\gamma = 1.73$ sample using X-ray diffraction (not shown for brevity) and a good match was found between the results obtained by the two techniques.

The texture of the initial material was characterized by a $\langle 10\bar{1}0\rangle \| Z$ type partial fibre with moderate strength (Fig. 13). At the same time, the $c$-axis is perpendicular to the longitudinal axis of the bar (see the $(0002)$ pole figure). The main ideal end orientation for hcp materials subjected to simple shear (torsion) is the B fibre [12,13] (see Fig. 14 for the ideal orientations). The initial texture fibre was far, at ~90° from the B fibre (with respect to the main texture evolution feature, i.e. rotation around the radial axis of the bar [13]). Consequently, under applied shear there is a progressive anticlockwise rotation of the texture around the radial axis towards that of the B fibre. However, for a shear strain of $\gamma = 1.73$ the position of the maximum in the experimental texture is still located ~40° from that of the B fibre, with a slight increase in texture intensity. Clearly, a shear strain of 1.73 is not enough to reach the ideal fibre for the present initial material.

### 3.4. Deformation texture simulations

Deformation texture simulations were carried out using the VPSC code developed by Lebensohn and Tomé [40] (Version 7). DRX was not taken into account in the simulations. Consequently, the influence of DRX can be considered as the deviation between the experimental and

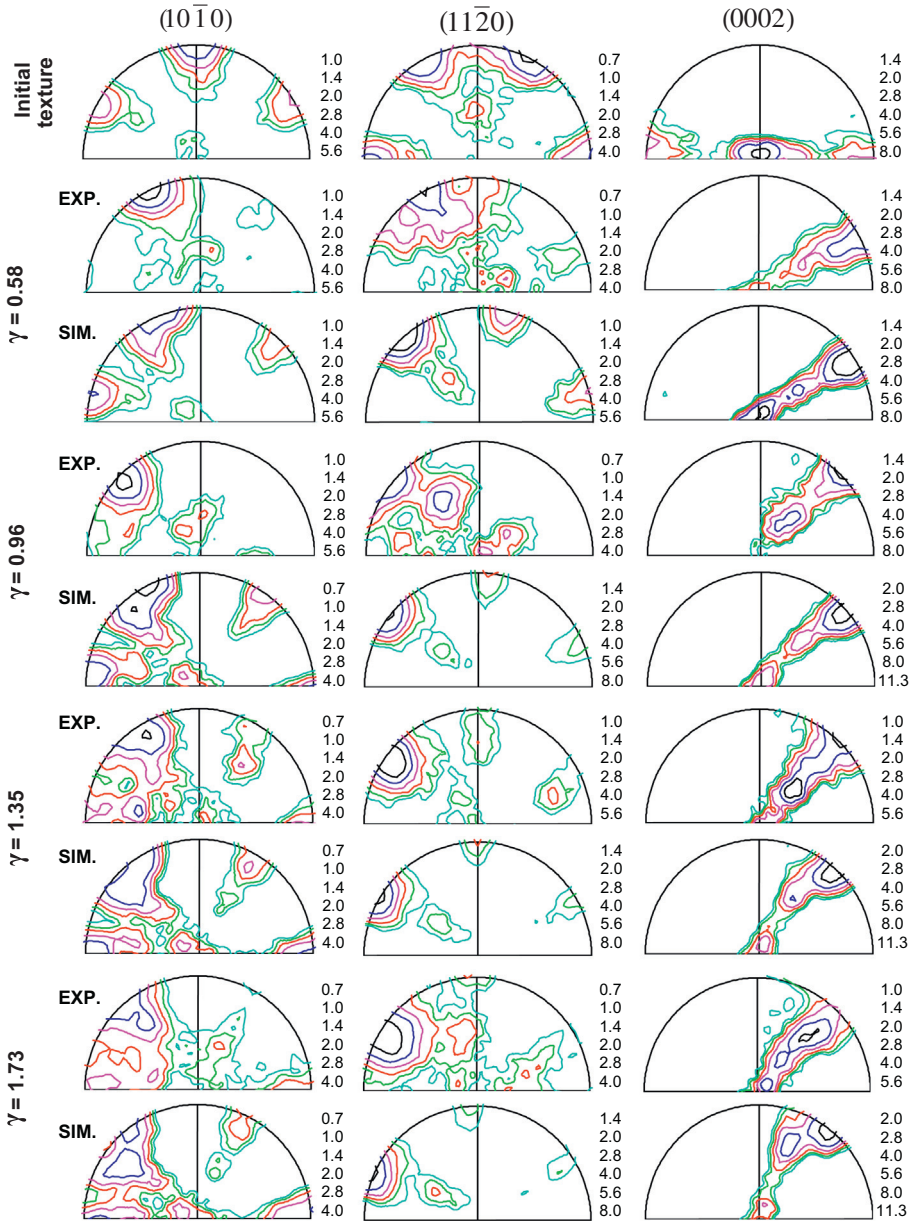


Fig. 13. (10$\bar{1}$0), (11$\bar{2}$0) and (0002) pole figures as a function of strain obtained experimentally and by simulation ($\theta$ on the right, $Z$ at the top, with $R$ being the projection plane).

simulated textures. The initial texture measured by EBSD was used to generate the input grain orientations of about 2000 grains for the simulations. The following families of slip systems were used in the simulations: basal $\{0001\}\langle 11\bar{2}0\rangle$, prismatic $\{1\bar{1}00\}\langle 11\bar{2}0\rangle$, pyramidal $\langle a\rangle\{10\bar{1}1\}\langle 11\bar{2}0\rangle$, pyramidal $\langle c+a\rangle$ type I $\{10\bar{1}1\}\langle 11\bar{2}3\rangle$ and pyramidal $\langle c+a\rangle$type II $\{11\bar{2}2\}\langle 11\bar{2}3\rangle$. Several sets of reference strengths were considered for these slip families and the one that best corresponded to the experimental observations was selected, $\left[\tau_0^{\text{basal}}/\tau_0^{\text{prism}}/\tau_0^{\text{pyr}\langle a\rangle}/\tau_0^{\text{pyr}\langle c+a\rangle\text{I}}/\tau_0^{\text{pyr}\langle c+a\rangle\text{II}}\right]$: (15/105/105/67/67), where the values in parentheses are in MPa. Deformation twinning was not considered in the simulations since negligible twin fractions were observed in the EBSD measurements. This is also in accordance with the literature, in which it has been reported that twinning activity in magnesium can be neglected at high homologous temperatures [41,42]. Our relative frequency measurements on twinning corroborate this finding (see Fig. 11). As for the strain rate sensitivity parameter of slip, a value of $m = 0.2$ was selected, in agreement with our measurements at 250 °C (see also Asaro and Needleman [43], Neale et al. [44], Vander Giessen et al. [45] and Tóth et al. [46]). The constitutive law of rate sensitive slip proposed by Hutchinson [47] was used in the VPSC simulations:

$$\tau^{s,f} = \tau_0^f \operatorname{sgn}(\dot{\gamma}^{s,f})\left|\frac{\dot{\gamma}^{s,f}}{\dot{\gamma}_0}\right|^m = \tau_0^f \frac{\dot{\gamma}^{s,f}}{\dot{\gamma}_0}\left|\frac{\dot{\gamma}^{s,f}}{\dot{\gamma}_0}\right|^{m-1} \tag{4}$$

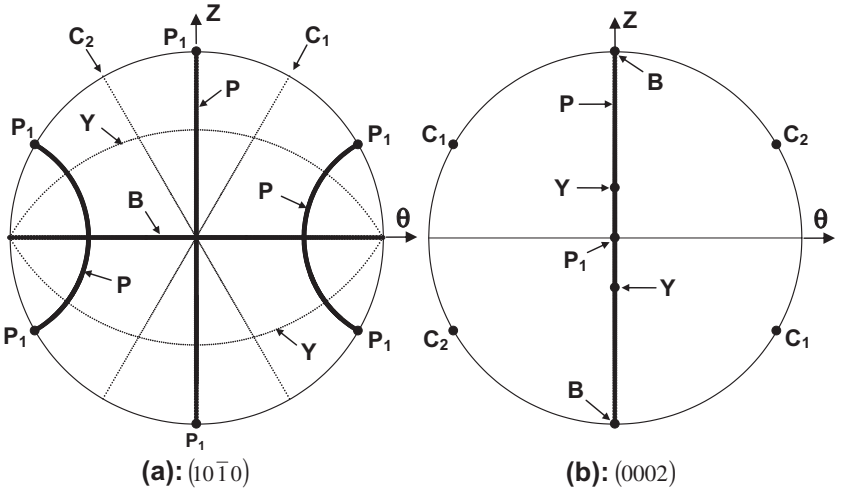


Fig. 14. Ideal orientations for magnesium under simple shear as they appear in the (a) (10$\bar{1}$0) and (b) (0002) pole figures [12]. The fibres are: B, basal; P, prismatic; Y, pyramidal I; $C_1$ and $C_2$, pyramidal II.

Here $\tau^{s,f}$ is the resolved shear stress in the slip system $s$ of the family indexed by $f$, $\dot{\gamma}^{s,f}$ is the slip rate, and $\tau_0^f$ is the reference stress level (at which the slip rate is $\dot{\gamma}_0$). The reference shear rate $\dot{\gamma}_0$ was assumed to be the same for all slip systems. It is also assumed here that the reference shear stress $\tau_0^f$ was the same within a given slip system family, but could differ from one family to another. Slip system hardening due to deformation was not modelled as it was already accounted for by textural hardening (see below). As a reference system for the Euler angles of the hexagonal crystal a Cartesian system was fixed to the unit cell so that the $x$, $y$ and $z$ axes of testing were parallel to the non-rotated [10$\bar{1}$0], [11$\bar{2}$0] and [0002] crystallographic axes, respectively. The simulations were carried out for simple shear, i.e. the experimentally observed slight shortening of the sample (Swift effect) was neglected. The simulation results are presented along with the experimental ones in Fig. 13 for increasing strain. Interestingly, in spite of not modelling any restoration process (dynamic recovery or recrystallization) the experimental results were quite well reproduced in all cases, including the rotation of the texture. The reasons for this will be discussed in Section 3.5.

Fig. 4 shows the strain–stress curves obtained from the simulations. Note that strain hardening was not simulated, so any hardening originated from texture evolution. At a strain of $\gamma = 0.96$ softening occurred, which was also captured in the simulation, however the rate of softening in the simulation was lower. It is reasonable to assume that the difference might be due to the occurrence of DRX. Indeed, the number of small grains generated by DRX was more than 35% at $\gamma = 0.96$ (see Fig. 8).

In order to obtain more information about hardening or softening induced by evolution of the texture, the activities of the slip systems were also examined (Fig. 15). As can be seen, there were significant variations in activation of the different slip families as a function of strain. Basal slip decreased from an initial activity of 85% to 32% at a shear of 1.0, while the activity of the pyramidal slip systems increased. Prismatic and pyramidal $\langle a \rangle$ slip contributed less than 10% to the total slip. Thus the observed hardening is due to increased activity of the harder slip systems, which become more active as a consequence of the evolution of the texture. The initial enhancement of pyramidal slip introduces initial hardening, while an increase in basal glide leads to softening at $\gamma = 0.96$, as shown in the simulated curves. A similar effect was observed and simulated in previous works on AZ31 [13,48] without hardening and at room temperature. The only difference from the present investigation was that twinning had to be taken into account in those studies [13,48] due to the lower deformation temperature.

### 3.5. Dynamic recrystallization mechanism

As can be seen in Fig. 5, the minimum of the second derivative of the strain hardening curve occurred at $\tau =$ 50 MPa, indicating the onset of dynamic restoration, which corresponds to a relatively small amount of plastic strain of

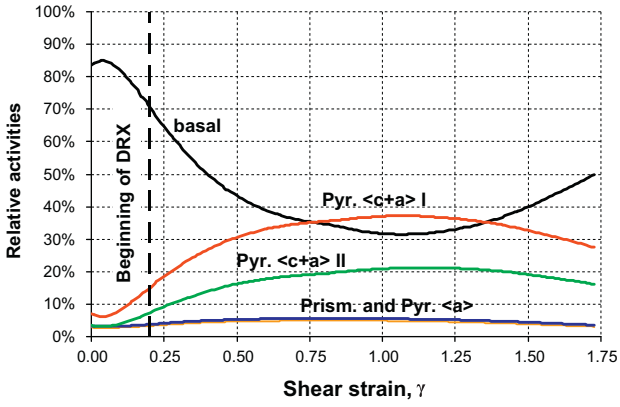


Fig. 15. Simulated relative activities of the slip system families.

$\gamma = 0.2$ (Fig. 4). The microstructure of the specimen for a strain level of $\gamma = 0.38$ clearly shows the presence of small equiaxed grains surrounding the much larger elongated deformed grains (Fig. 6). At this strain the area fraction of these equiaxed dynamically recrystallized grains was estimated to be ~10% (Fig. 8). The overall increase in HAGBs (Fig. 11) with deformation is an indication of an increase in the fraction of dynamically recrystallized grains. This could be corroborated from Fig. 8 showing the area fraction of dynamically recrystallized grains as well as the number of dynamically recrystallized grains per unit of deformed grains (Fig. 9). With an increase in strain dynamically recrystallized grains form, subsequently grow and deform with further deformation.

In order to determine the mechanism of DRX magnified views of the EBSD scans were analysed. It is important to know whether the DRX observed is orientation dependent in the Mg alloy AM30, as it is in pure Mg. Thus the orientation dependence of the DRX mechanism was compared with an earlier investigation on pure magnesium [20]. Two representative scans are shown in Fig. 16 from two locations having different crystallographic planes nearly parallel to the $\theta$–$Z$ plane at a strain of $\gamma = 0.77$. These planes are prismatic/pyramidal (Fig. 16a–c) and near basal (Fig. 16d–f). In these maps the boundary disorientations were differentiated for three different ranges: 2–5° (in red) corresponding to very low angle boundaries (VLABs), 5–15°5°–5°(in green) for LAGBs and >15° (in blue or black) for HAGBs. It can be observed that most of the VLABs and LAGBs are in the vicinity of HAGBs (Fig. 16a and d). Their concentration decreases towards the centre of the original grains. A careful observation reveals that nearer to the HAGBs VLABs are converted into LAGBs and form cells and subgrain boundaries. Finally, these subgrains are converted into HAGBs to form new grains, which could be associated with the process termed "continuous dynamic recovery and recrystallization" (CDRR) [49]. However, even if LAGBs are converted to HAGBs at the boundaries of the deformed grains, there is the possibility of nucleation of new grains with different orientations to the parent grain, as occurs during DDRX. In order to examine the differences in orientation between the deformed grains and the surrounding recrystallized grains IPFs with a superimposed hcp unit cell was constructed for almost every grain (Fig. 16c and f). It can be observed that the unit cells of the recrystallized grains are rotated by ~30° around their $c$-axis compared with the deformed grains in almost all cases (Fig. 16c).

Earlier it was suggested [15] that at higher deformation temperatures the contribution of non-basal slip is quite significant, leading to more homogeneous deformation, which might promote DDRX. However, it has recently been

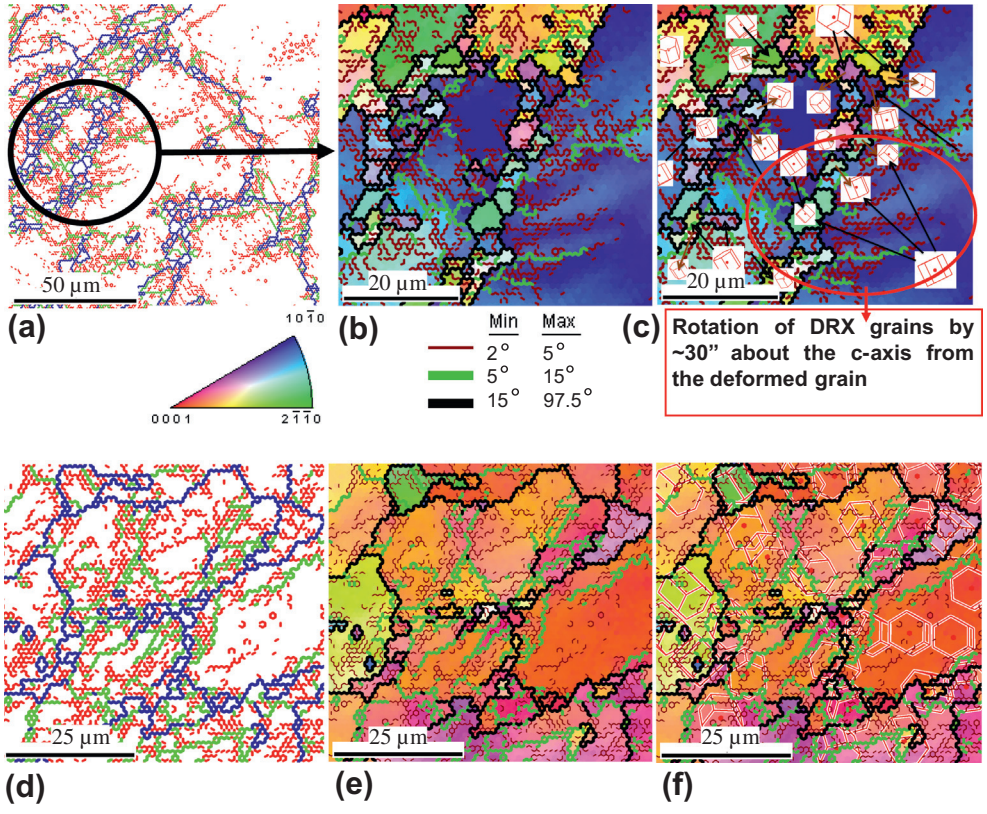


Fig. 16. Magnified grain boundary and inverse pole figures with superimposed unit cells showing (a–c) prismatic/pyramidal and (d–f) near basal crystallographic planes parallel to the $\theta$–$Z$ sample plane after a strain of $\gamma = 0.77$. (c, f) The change in orientation (rotation of the hcp unit cell) leading to the formation of 2–5° and 5–15° LAGBs and, subsequently, (a, d) DRX grains with ~30° rotation along the $c$ axis, which can be visualized from the geometric centre of the deformed grain.

shown [20] that during equal channel angular extrusion of pure magnesium CDRR was predominant when microstructure on the prismatic/pyramidal planes was observed, while on sections oriented near basal planes DDRX was reported. It was suggested that the difference in stacking fault energies (SFE) between the basal and non-basal planes is responsible for the difference in the observed DRX mechanisms. For pure magnesium the SFE of the basal plane is ~32 mJ $m^{-2}$ and those of the prismatic and pyramidal planes are ~265 and ~344 mJ $m^{-2}$, respectively [50]. In the present investigation CDRR was observed in all cases, irrespective of the orientation of the deformed grains. The authors believe that dilute addition of aluminium, manganese and zinc to magnesium leads to a normalization of the differences in SFE of different crystallographic planes. This would lead to an overall medium high SFE (for both basal and non-basal planes) in this Mg–Al alloy, which might trigger CDRR.

Our understanding of the development of CDRR is illustrated schematically in Fig. 17. Due to the shear deformation applied to the initially equiaxed microstructure (Fig. 17a) the grains elongate and new dynamically recrystallized grains form at the grain boundaries (Fig. 17b). With further deformation a necklace structure develops (Fig. 17c), which thickens with subsequent deformation (see Fig. 6).

Fig. 17d is a magnified image of the initial grain shown in Fig. 17a, which may contain some misorientations in the form of VLAGBs (red) and LAGBs (green). On shear deformation the grains elongate and dislocations pile up at the grain boundaries (HAGBs in blue). The concentration of misorientations increases in the vicinity of HAGBs (see Fig. 17e, shown experimentally in Fig. 16a and d). Fig. 17f is a magnified version of Fig. 17b. The newly formed dynamically recrystallized grains subsequently deform with an increase in strain (Fig. 17g). Due to the increase in the number of dynamically recrystallized grains they form a necklace structure (Fig. 17h).

Ponge et al. [51] have shown that the initiation of DRX is preceded by fluctuations in the grain boundary growth shape. Serrations and bulges develop, and eventually new grains are generated along these grain boundaries. Fig. 17i–k shows the mechanism of formation of serrations at the grain boundaries. It is well known that geometrically necessary dislocations (GND) and statistically stored dislocations (SSD) are formed during deformation [52,53]. A minimum density of non-polar dislocations, i.e. SSDs, are required for deformation to be sustained. However, these SSDs do not contribute to misorientations in the grain. On the other hand, polar dislocations (GNDs) slip and cluster together to increase misorientation inside the grains [54]. The presence of misorientations near a grain boundary in the initial microstructure is schematically represented in Fig. 17i. Clusters of GNDs are subsequently formed in the vicinity of grain boundaries, forming misorientations within the grains (see Fig. 16) [55,56].

Due to the applied shear the grain boundaries tend to rotate around the radial axis (see Fig. 6c). This rotation cannot occur "homogenously" (Fig. 17j), but instead forms

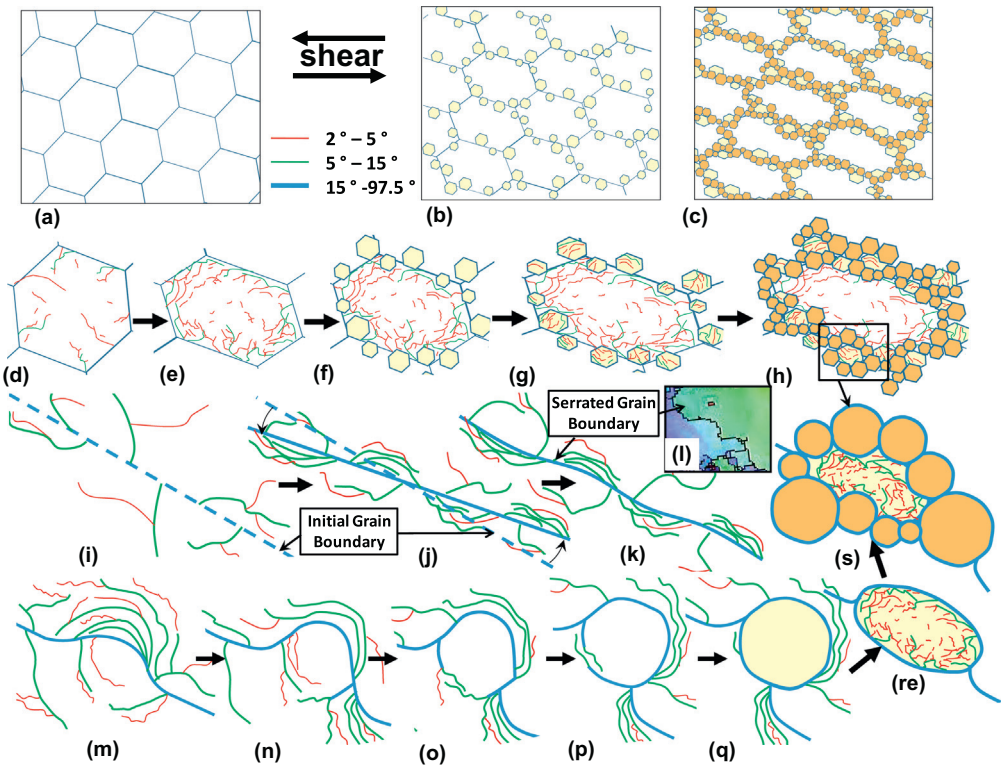


Fig. 17. Schematic showing the mechanism of dynamic recrystallization during continuous deformation by shear.

serrated boundaries (Fig. 17k). Further GNDs are generated near the grain boundaries to accommodate this deformation and to maintain the grain boundary compatibility. These GNDs are generated inhomogeneously at the grain boundaries [56] and are related to the slip system activity and strain in regions separated by the misorientations [57]. GND densities become heterogeneous in the vicinity of grain boundaries (Fig. 17j) [58], as observed in Fig. 16. When the density of dislocations entering the grain boundaries exceeds their absorption capacity or when the process of dislocation absorption requires an incubation time the grain boundaries become serrated [59], as shown in Fig. 17k. In other words, the high number of dislocation pile-ups and subsequent high local stress concentrations at the grain boundaries result in the formation of serrated grain boundaries. Fig. 17l shows a magnified view of a serrated grain boundary.

With further deformation bulging develops (Fig. 17m and n). At the same time GNDs evolve in the vicinity of grain boundaries, leading to increasing numbers of VLAGB misorientations becoming to LAGBs [60] and, finally, HAGBs (Fig. 17m–p) [61], with new recrystallized grains being formed (Fig. 17q). The new DRX grains were subsequently deformed, became elongated, and new misorientations developed (Fig. 17r). The second stage of CDRR is shown in Fig. 17s, following the same mechanism as in Fig. 17i–q.

In this way a necklace structure develops. Independent studies [15–18] have revealed that in magnesium progressive lattice rotation takes place due to local shearing near the grain boundaries due to the lack of five independent slip systems. However, the present investigation reveals the occurrence of CDRR, while non-basal slip systems are active, so that there are at least five active slip systems. Lattice curvatures are commonly observed near grain boundaries, which eventually lead to CDRR. A grain fragmentation model was recently proposed [62] in which lattice curvature is attributed to slowdown of the rotation of the crystal lattice near the grain boundary.

### 3.6. Effect of DRX on texture evolution

Following analysis of the microstructures presented above it could be estimated that the occurrence of CDRR in the present Mg alloy during torsion deformation involves an orientation change of ~30° around the basal axis. However, in spite of the occurrence of DRX, the main features of texture evolution could be satisfactorily reproduced by VPSC simulations without taking into account any recrystallization process. This apparent contradiction will be resolved in the following.

In order to obtain a better understanding of texture evolution during dynamic recrystallization the measured orientation distribution functions (ODFs) are represented in the $\varphi = 90°$ orientation space in the left column of Fig. 18 as a function of strain. A projection of the rotation field $\dot{g} = (\dot{\phi}_1, \dot{\phi}, \dot{\phi}_2)$ (white arrows) is also plotted for the initial texture, to illustrate the tendencies in evolution of the texture (for more details on the rotation field, see Tóth et al. [46,63] and Gilormini et al. [64]).

The starting material displays a fibre texture in Euler space oriented at $(\varphi_1,\varphi,\varphi_2) = (90°,90°,0–60°)$ with maxima at (90°,90°,0°) and (90°,90°,60°) (these are equivalent orientations). As can be seen, the main trend of texture evolution is a rotation in the direction of rigid body spin (in the direction of the $\varphi_1$ axis, which corresponds to rotation around the radial direction of the bar with the final parameters of the B fibre, which is located at ($\varphi_1 = 0$ or 180°, $\varphi = 90°$, $\varphi_2 = 0–60°$). Note that the lattice rotation spin around the $R$ axis ($\dot{\phi}_1$) is not uniform in the $\varphi = 90°$ section and is maximum along the $\varphi_1 = 90°$ line. At this location ($\varphi_1 = 90°$, $\varphi = 90°$, $\varphi_2 = 0°$) the lattice rotation is about twice as great as the rigid body spin (this peculiarity of rotation in hexagonal crystals has been reported and explained by Beausir et al. [12]). This is the reason why rotation of the texture is initially so high around the $R$ axis, ~15° for a shear strain of only $\gamma = 0.38$ and ~5° during the next strain increment $\gamma = 0.58$. Rotation continues along $\varphi_1$ during the next two strain increments, but practically stops at $\gamma = 0.96$. The final position of the fibre is located at $\varphi_1 = 140°$ at a strain of $\gamma = 1.73$. A further 40° rotation would be needed to reach the ideal orientation.

In order to visualize the differences between the deformation texture due to torsion and the texture due to DRX $\varphi = 90°$ sections of the ODF for the partitioned equiaxed grains surrounding the elongated deformed grains are presented in the right column of Fig. 18. For $\gamma = 0.38$ the texture of the dynamically recrystallized region is almost identical to the overall texture, with a somewhat greater spread. At $\gamma = 0.58$ the fibre intensity is highest at $\varphi_2 = 30°$, and a more homogeneous fibre located at $(\varphi_1,\varphi,\varphi_2) = (110°,90°,0–60°)$ forms. This fibre persists at $\gamma = 0.77$, with the shift in texture along $\varphi_1$ being associated with shearing. With the increase in strain ($\gamma = 0.96$, 1.15, 1.35 and 1.73) a more intensified texture forms at $(\varphi_1,\varphi,\varphi_2) = (140°,90°,30°)$, evidence of a rotation of 30° around the $c$-axis, which corroborates our analysis based on the microstructure in the previous section.

The variations in the ODF due to DRX can be interpreted using plastic power. As proposed earlier [65], the DRX process is controlled by the plastic power in a grain $g$ and is defined as:

$$E(g) = \sum_f \sum_s \tau^{s,f}(g)\dot{\gamma}^{s,f}(g) \tag{5}$$

The plastic power was plotted over the entire Euler space on a grid separated by 1° using the viscoplastic self-consistent approach for a small strain increment (0.01) (see the plastic power map for $\varphi = 90°$ in Fig. 18, right column, top). DRX grains are expected to appear at locations in the orientation space which correspond to the minimum plastic power position. By comparing the energy map and the ODFs of the partitioned dynamically recrystallized grains it can be seen that formation of the

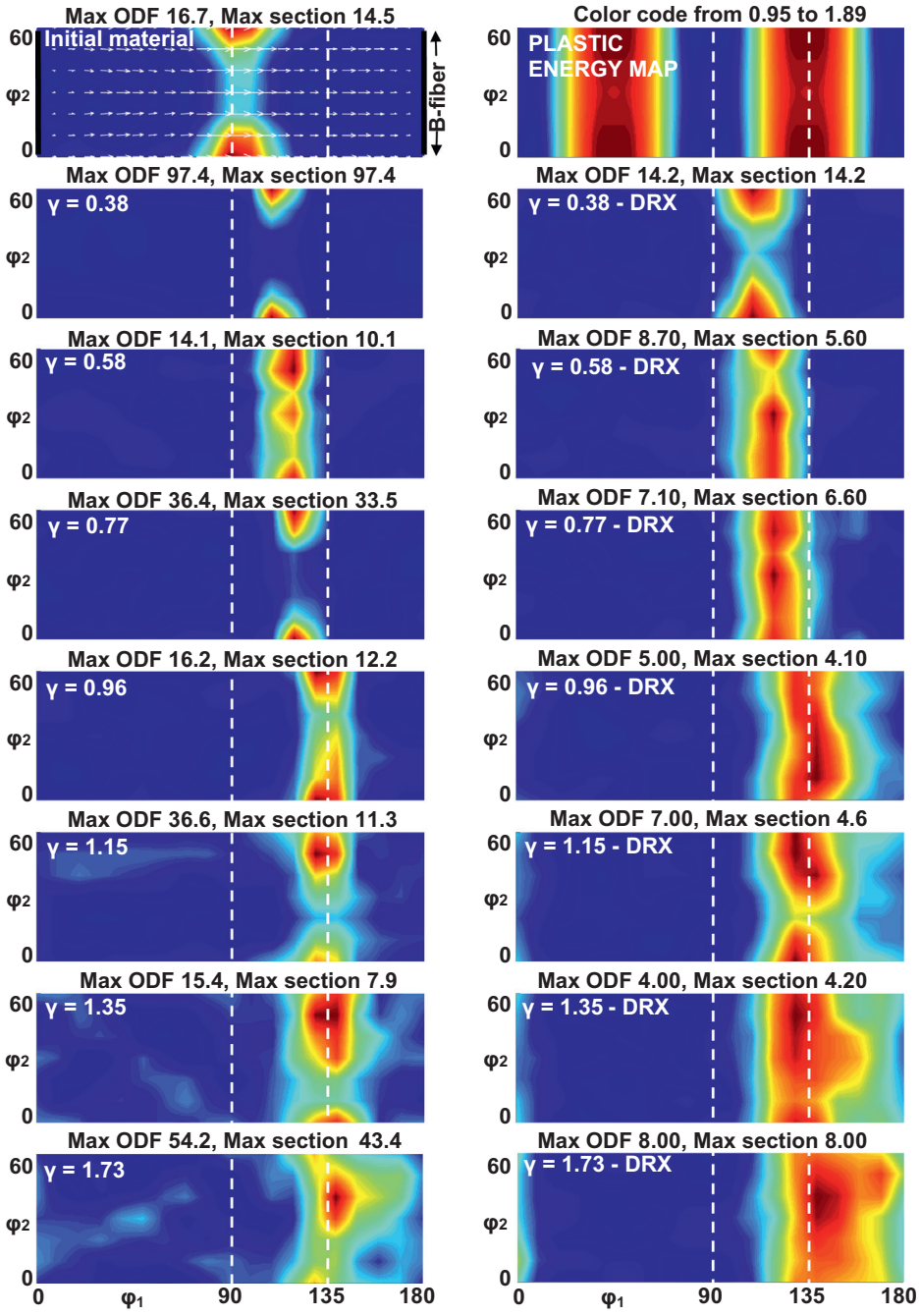


Fig. 18. $\varphi = 90°$ ODF sections of the measured textures (left column) and for the DRX grains only (right column) as a function of strain and the corresponding energy map (top right).

DRX texture indeed follows the local minimum energy orientations. This tendency can be clearly identified in Fig. 18, with an exception at a shear strain of $\gamma = 0.32$. This, however, can be explained using again the plastic power map. At this location in Euler space ($\varphi_1 \approx 110°$) the plastic power is constant along the $\varphi_2$ axis, so no preference is expected for the location in $\varphi_2$. Further strain is needed to rotate the texture into the region where a local minimum in plastic power appears at $\varphi_2 = 30°$.

An explanation as to why the texture does not reach the ideal position is still needed. For this purpose it is necessary to study the variations in lattice spin, which were represented by the so-called persistence parameter in the study of Beausir et al. [12]. According to that study there are ideal positions of the texture along the fibre line $(\varphi_1,\varphi,\varphi_2) = (120°,90°,0–60°)$ which relate to the activity of $\langle c + a \rangle$ slip. The lattice rotation, however, is not zero at that position, only decreasing temporarily, which results in a slowdown of rotation of the texture. This slowdown and the limited amount of strain finally lead to the observed texture. Note that the simulation faithfully reproduces the position of the experimental texture (Fig. 13).

The occurrence of DRX according to the mechanism of 30° rotation around the *c*-axis does not significantly influence the texture, because it transfers orientations along the fibre. This is the reason why the simulation could reproduce the correct fibre orientation without taking into account DRX.

## 4. Conclusions

Torsion tests were carried out at 250 °C at a strain rate of $7.5 \times 10^{-4}\ s^{-1}$ up to a maximum shear strain of 1.73. The evolution of the microstructure and the texture were monitored as a function of strain. The analyses of the results have led to the following main conclusions.

1. Partial DRX took place during deformation, resulting in a necklace structure. The microstructure displayed a bimodal grain size distribution.
2. The orientation difference of the newly formed grains compared with the deformed grains and the evolution of HAGBs due to the transformation of LAGBs suggest that the mechanism of DRX is continuous dynamic recovery and recrystallization in the magnesium alloy AM30 at 250 °C.
3. The texture of the partitioned dynamically recrystallized grains indicated that the DRX process is governed by the plastic power.
4. Evolution of the experimental texture was faithfully reproduced using the VPSC polycrystal code and was interpreted with the help of the persistence characteristics of shear textures previously established in Beausir et al. [12].

## Acknowledgements

S.B. acknowledges prolific discussions with Prof. R.K. Ray. The authors acknowledge Prof. Atul Choksi (IISc Bangalore) for providing the alloy for the present study. This work was supported by the French State through the program "Investment in the future" operated by the National Research Agency (ANR-11-LABX-0008-01 (LabEx DAMAS)). This work also involved use of the facility set up under the Institute of Nanoscience Initiative sponsored by the DST-FIST program at IISc, Bangalore.

## References

[1] Stalmann A, Sebastian W, Friedrich H, Schumann S, Dröder K. Adv Eng Mat 2001;3:969.
[2] Kainer KU, Von Buch F. In: Kainer KU, editor. Magnesium alloys and technologies. Weinheim: DGM; 2003. p. 1.
[3] Toth LS, Jonas JJ, Daniel D, Bailey JA. Text Microstruct 1992;19:245.
[4] Van Houtte P, Aernouldt E, Sekine K. In: Nagashima S, editor. Proceedings of ICOTOM 6. Tokyo: ISIJ; 1981. p. 337.
[5] Montheillet F, Cohen M, Jonas JJ. Acta Metall 1984;32:2077.
[6] Hughes DA, Wenk HR. In: Kallend JS, Gottstein G (eds.), Proceedings of ICOTOM 8. Santa Fe NM 1988, p. 455.
[7] Böhlke T, Bertram A, Krempl E. Int J Plasticity 2002;19:1867.
[8] Duchêne L, El Houdaigui F, Habraken AM. Int J Plasticity 2007;23:1417.
[9] Sanchez P, Pochenttino A, Chauveau T, Bacroix B. J. Nuclear Mater 2001;298:329.
[10] Evans WJ, Jones JP, Whittaker MT. Int J Fatigue 2005;27:1244.
[11] Balasubramanian S, Anand L. Acta Mater 2002;50:133.
[12] Beausir B, Toth LS, Neale KW. Acta Mater 2007;55:2695.
[13] Beausir B, Toth LS, Qods F, Neale KW. J Eng Mater Technol 2009;131. 011108-1.
[14] Myshlyaev MM, McQueen HJ, Mwembela A, Konopleva E. Mater Sci Eng A 2002;337:121.
[15] Ion SE, Humphreys FJ, White SH. Acta Metall 1982;30:1909.
[16] Galiyev A, Kaibyshev R, Gottstein G. Acta Mater 2001;49:1199.
[17] Tan JC, Tan MY. Mater Sci Eng A 2003;339:124.
[18] Humphreys FJ, Hatherly M. Recrystallization and related annealing phenomena. 2nd ed. Oxford: Elsevier; 2004. p. 438.
[19] Mwembela A, Konopleva EB, McQueen HJ. Scripta Mater 1997;37:1789.
[20] Biswas S, Dhinwal SS, Suwas S. Acta Mater 2010;58:3247.
[21] Del Valle JA, Ruano OA. Mater Sci Eng A 2008;487:473.
[22] Gehrman R, Gottstein G. In: Szpuner JA, editor. Proceedings of ICOTOM 12. Montreal: NRC Research Press; 1999. p. 670.
[23] Engler O. Metall Mater Trans A 1999;30:1517.
[24] Humphreys FJ, Kalu PN. Text Microstruct 1990;703:14.
[25] Hatherly M, Hutchinson WB. An introduction to textures in metals. London: Chameleon Press; 1990.
[26] Bache MR, Evans WJ. Mater Sci Eng A 2001;409:319–21.
[27] Nadella RK, Samajdar I, Gottstein G. In: Kainer KU, editor. Proceedings of magnesium alloys applications. Weinheim: Wiley VCH; 2003. p. 1052.
[28] Biswas S, Dhinwal SS. Suwas S. In: Haldar A, Suwas S, Bhattacharjee D, editors. Proceedings of the international conference microstructure and texture in steels and other materials. London: Springer-Verlag; 2009. p. 465.
[29] Suwas S, Ray RK. Acta Mater 1999;18:4599.
[30] Suwas S, Ray RK, Singh AK, Bhargava S. Acta Mater 1999;47:4585.
[31] Wagner F, Bozzolo N, Van Landuyt O, Grosdidier T. Acta Mater 2002;50:1245.
[32] Swift HW. Engineering 1947;4:253.
[33] Neale KW, Schrivastava SC. Eng Fract Mech 1985;21:747.
[34] Fields DS, Backofen WA. Proc ASTM 1957;57:1259.
[35] Agnew SR, Duygulu O. Int J Plasticity 2005;21:1161.
[36] Kim WJ, Chung SW, Chung CS, Kum D. Acta Mater 2001;49:3337.
[37] Poliak EI, Jonas JJ. Acta Mater 1996;44:127.
[38] Canova GR, Kocks UF, Jonas JJ. Acta Metall 1984;32:211.
[39] Samman TA, Gottstein G. Mater Sci Eng A 2008;448:406.
[40] Lebensohn RA, Tomé CN. Acta Metall 1993;41:2611.
[41] Barnett MR, Keshavarz Z, Beer AG, Atwell D. Acta Mater 2004;52:5093.
[42] Yang Q, Ghosh AK. Acta Mater 2006;54:5159.
[43] Asaro RJ, Needleman A. Acta Metall 1985;33:923.
[44] Neale KW, Toth LS, Jonas JJ. Int J Plasticity 1990;6:45.
[45] Vander Giessen E, Wu PD, Neale KW. Int J Plasticity 1992;8:773.
[46] Toth LS, Gilormini P, Jonas JJ. Acta Metall 1988;36:3077.
[47] Hutchinson JW, Proc R. Soc Lond 1976;101:127.
[48] Staroselsky A, Anand L. Int J Plasticity 2003;19:1843.
[49] Jin L, Lin D, Mao D, Zeng X, Bin Chen B, Ding W. Mater Sci Eng A 2006;423:247.
[50] Smith AE. Surf Sci 2007;601:5762.
[51] Ponge D, Gottstein G. Acta Mater 1998;46:80.
[52] Nye JF. Acta Metall 1953;1:153.
[53] Ashby MF. Phil Mag 1970;21:399.
[54] Arsenlis A, Parks DM. Acta Mater 1999;47:1597.
[55] Hornbogen E. Metall Trans A 1979;10:947.
[56] Kuhlmann-Wilsdorf, Hansen N. Scripta Mater 1991;25:1557.
[57] Kassner ME, D Barrabes RS. Mater Sci Eng A 2005;410/411:152.
[58] Doherty RD, Hughes DA, Humphreys FJ, Jonas JJ, Juul Jensen D, Kassnerf ME, et al. Mater Sci Eng A 1997;238:219.

[59] Valiev RZ, Kaibyshev OA, Khannanov Sh Kh. Phys Status Solidi A 1979;52:447.
[60] Hales HJ, McNelley TR, McQueen HJ. Metall Trans A 1991;22:1037.
[61] Doherty RD, Gottstein G, Hirsch J, Hutchinson WB, Lucke K, Nes E, Wilbrandt PJ. G. In: Kallend JS, Gottstein G (eds.), Proceedings of ICOTOM 8. Santa Fe NM 1988, p. 563.
[62] Toth LS, Estrin Y, Lapovok R, Gu CF. Acta Mater 2010;58:1782.
[63] Toth LS, Jonas JJ, Neale KW. Proc R Soc Lond A 1990;427:201.
[64] Gilormini P, Toth LS, Jonas JJ. Proc R Soc Lond A 1990;430:489.
[65] Beausir B, Biswas S, Kim DI, Toth LS, Suwas S. Acta Mater 2009;57:5061.